frontiers | Frontiers in Chemistry

TYPE Original Research
PUBLISHED 15 September 2022
DOI 10.3389/fchem.2022.996084

OPEN ACCESS

EDITED BY
Ligang Feng,
Yangzhou University, China

REVIEWED BY
Zhenghua Tang,
South China University of Technology, China
Guoxing Zhu,
Jiangsu University, China

*CORRESPONDENCE
Fengxiang Yin,
yinfx@cczu.edu.cn

†These authors have contributed equally to this work

SPECIALTY SECTION
This article was submitted to Electrochemistry, a section of the journal Frontiers in Chemistry

RECEIVED 17 July 2022
ACCEPTED 25 August 2022
PUBLISHED 15 September 2022

CITATION
He X, Dong Y, Yin F, Li G and Zhao X (2022), $NiCo_2O_4$ nanoparticles rich in oxygen vacancies: Salt-Assisted preparation and boosted water splitting. *Front. Chem.* 10:996084. doi: 10.3389/fchem.2022.996084

$NiCo_2O_4$ nanoparticles rich in oxygen vacancies: Salt-Assisted preparation and boosted water splitting

Xiaobo He[1†], Yuanchu Dong[1†], Fengxiang Yin[1*], Guoru Li[1] and Xinran Zhao[2]

[1]Jiangsu Key Laboratory of Advanced Catalytic Materials and Technology, School of Petrochemical Engineering, Changzhou University, Changzhou, China, [2]College of Chemical Engineering, Beijing University of Chemical Technology, Beijing, China

$NiCo_2O_4$ is a promising catalyst toward water splitting to hydrogen. However, low conductivity and limited active sites on the surfaces hinder the practical applications of $NiCo_2O_4$ in water splitting. Herein, small sized $NiCo_2O_4$ nanoparticles rich in oxygen vacancies were prepared by a simple salt-assisted method. Under the assistance of KCl, the formed $NiCo_2O_4$ nanoparticles have abundant oxygen vacancies, which can increase surface active sites and improve charge transfer efficiency. In addition, KCl can effectively limit the growth of $NiCo_2O_4$, and thus reduces its size. In comparison with $NiCo_2O_4$ without the assistance of KCl, both the richer oxygen vacancies and the reduced nanoparticle sizes are favorable for the optimal $NiCo_2O_4$-2KCl to expose more active sites and increase electrochemical active surface area. As a result, it needs only the overpotentials of 129 and 304 mV to drive hydrogen and oxygen evolution at 10 mA cm^{-2} in 1 M KOH, respectively. When $NiCo_2O_4$-2KCl is applied in a symmetrical water splitting cell, a voltage of ~1.66 V is only required to achieve the current density of 10 mA cm^{-2}. This work shows that the salt-assisted method is an efficient method of developing highly active catalysts toward water splitting to hydrogen.

KEYWORDS

salt-assisted method, spinel, hydrogen evolution reaction, oxygen evolution reaction, water splitting

1 Introduction

Hydrogen is not only an important raw material, but also a fuel with high energy density (Tenhumberg and Büker, 2020; Hjeij et al., 2022; Lee et al., 2022). However, most of commercial hydrogen production technologies are accompanied by massive carbon dioxide emissions (Dawood et al., 2020). Among the recently-developed green methods to hydrogen, electrochemical water splitting in alkaline conditions has attracted much attention (Wang et al., 2019; Cao et al., 2020; Yu et al., 2021), due to its zero emission, high purity of the produced hydrogen and abundant sources.

Electrochemical water splitting contains two half reactions: cathodic hydrogen evolution reaction (HER) and anodic oxygen evolution reaction (OER) (Zhu et al., 2020a). Both HER and OER involve the transfer of multiple electrons and protons, thus resulting in slow kinetics. Highly active HER and OER catalysts are indispensable to promote water splitting to hydrogen fast and efficiently, especially bifunctional catalysts that can simultaneously accelerate HER and OER. Till now, Pt-based and Ir-based catalysts are the state-of-the-art HER and OER electrocatalysts, respectively (Zhang et al., 2022a; Kim et al., 2022). However, they are limited in large-scale production due to high costs and low reserves. In recent years, various Co-based electrocatalysts, such as phosphides (Zhang et al., 2022b), carbides (Wang et al., 2021), oxides (Jung et al., 2021) and sulfides (Dong et al., 2022) have been developed and applied for water splitting to hydrogen. Among them, $NiCo_2O_4$ spinel oxide has shown great application potentials in many energy storage and conversion systems (Chen et al., 2018; Ranjani et al., 2018), because of simple preparation methods, high stability against corrosion in electrochemical systems, and, more importantly, high electrochemical activity (Ha et al., 2019; Du et al., 2021; Sun et al., 2021). And also, it has been applied as highly efficient electrocatalysts in water splitting to hydrogen. For instance, He et al. developed $NiCo_2O_4$@FeP_x core-shell nanoneedle arrays grown on nickel foam (FeP-NCO@NF) as highly active bifunctional catalysts toward both HER and OER. The synergetic effects between $NiCo_2O_4$ and FeP_x resulted in the low HER (~82 mV) and OER (~220 mV) overpotentials and the low overall water-splitting voltage (~1.523 V) to deliver a current density of 10 mA cm^{-2} (He et al., 2021). Du et al. used *in-situ* deposition to control the loading of $NiCo_2O_4$ on the surface of Co_9S_8 by adjusting the number of deposition cycles (Du et al., 2021). The different loading of $NiCo_2O_4$ showed the different dominant activity toward HER and OER, respective. That is, Co_9S_8@$NiCo_2O_4$-70 cycles had the optimal OER activity, while Co_9S_8@$NiCo_2O_4$-10 cycles afforded the optimal HER activity. When they were coupled for overall water-splitting, Co_9S_8@$NiCo_2O_4$-70||Co_9S_8@$NiCo_2O_4$-10 displays a low voltage of ~1.55 V to drive the cell at 10 mA cm^{-2}. Further results demonstrated that $NiCo_2O_4$ promoted the adsorption and dissociation of water molecules in alkaline electrolytes.

Herein, this work has developed a salt (KCl)-assisted method to prepare $NiCo_2O_4$ nanoparticles as highly efficient catalysts toward HER, OER and overall water splitting. Recently, salt-assisted methods have been used to develop highly active catalysts towards electrocatalytic reactions (Li et al., 2020; Li et al., 2021a; Peng et al., 2021). Generally, salt-assisted methods have the two following main advantages. On one hand, the used salts can act as templates for the formation of porous (Li et al., 2021a) or specific nanostructures (Li et al., 2020). As a result, high specific surface areas have been achieved and the growth of nanostructures of catalysts can be tuned. On the other hand, it is favorable for salt-assisted methods to create abundant defects in catalysts (Peng et al., 2021), thus promoting the electrocatalytic processes.

Herein, the used KCl play important roles in tuning the structures of the resultant $NiCo_2O_4$, like other salts used in reports above (Li et al., 2020; Li et al., 2021a; Peng et al., 2021). As compared with $NiCo_2O_4$ without the assistance of KCl, the smaller-sized nanoparticles in the optimal $NiCo_2O_4$-2KCl are favorable to achieve the higher BET SSAs and expose more active sites and thus increase electrochemically active surface areas. Meanwhile, the KCl promotes the formation of abundant O_v in $NiCo_2O_4$-2KCl as well as $NiCo_2O_4$-1KCl and $NiCo_2O_4$-3KCl, and the more abundant O_v can also effectively improve the electrochemically active surface areas and enhance charge transfer efficiency during HER and OER. As a result, $NiCo_2O_4$-2KCl affords the much higher HER/OER bifunctional activity than $NiCo_2O_4$ without the assistance of KCl in alkaline electrolyte. Meanwhile, a cell consisting of $NiCo_2O_4$-2KCl||$NiCo_2O_4$-2KCl has the comparable overall water splitting performance to a 20 wt% Pt/C||IrO_2 cell.

2 Experimental

2.1 Preparation of catalysts

Figure 1 shows the whole preparation procedures of $NiCo_2O_4$ nanoparticles via the salt-assisted method. To prepare the typical $NiCo_2O_4$-2KCl, 29.55 g (0.1 mol) of $Co(NO_3)_2$•$6H_2O$, 59.34 g (0.2 mol) of $Ni(NO_3)_2$•$6H_2O$ were added into 320 ml of a aqueous solution of KOH (0.94 M) and stirred at room temperature for 1 h. Then, the suspension was transferred into a Teflon autoclave and heated at 200°C for 24 h. After naturally cooled to room temperature, the obtained NiCo precursor was washed by deionized water and absolute ethanol several times, and then was added into a saturated KCl solution that was prepared at 90°C by using 0.6 mol of KCl in advance. After stirring at 90°C for 30 min, a homogeneous suspension was formed, and then cooled to room temperature, filtered and dried at 60°C for the subsequent procedures. The obtained mixture consisting of NiCo precursor and KCl was annealed at 350°C in air for 2 h at a heating rate of 5°C min^{-1}. The obtained black solid powder was washed with deionized water and absolute ethanol for several times. After dried at 60°C, $NiCo_2O_4$ nanoparticles rich in oxygen vacancies was achieved. Meanwhile, $NiCo_2O_4$ without the assistance of KCl was prepared as a comparison. In addition, other $NiCo_2O_4$-*n*KCl (*n* = 1, 1.5, 3) samples were also synthesized via the similar salt-assisted procedures, where *n* represents the molar ratio of the fed amount of KCl and the total fed amount of Co and Ni (0.3 mol).

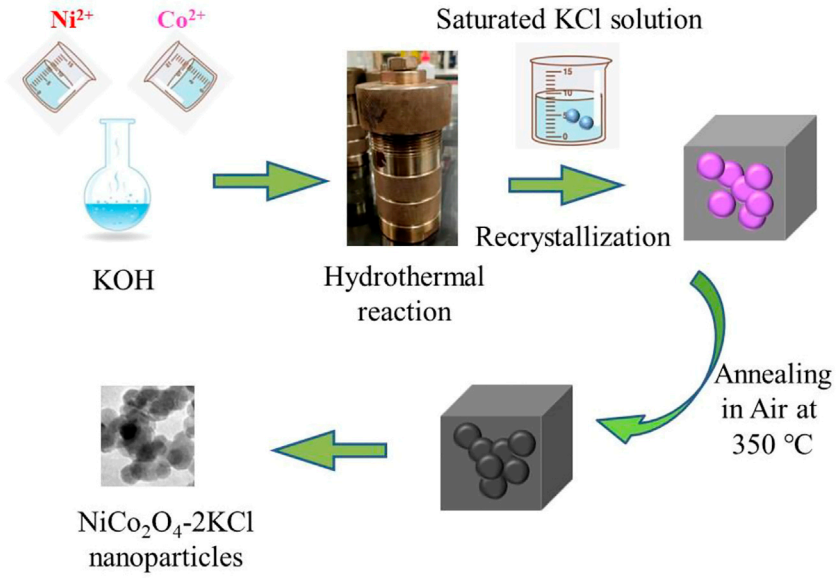

FIGURE 1
Schematic illustration of the salt-assisted preparation procedures of $NiCo_2O_4$.

2.2 Characterizations

X-ray powder diffraction (XRD) patterns were recorded on a diffractometer (D8 Advance, Bruker, Germany) with Cu K_α radiation (Cu K_α, λ = 1.5406 Å). X-ray photoelectron spectra (XPS) were collected on an ESCALAB 250XI XPS photoelectron spectrometer with an Al K_α X-ray resource (Thermo Fisher Scientific, United States) at a pass energy of 30 eV. The binding energy was referenced to the C 1s peak at 284.6 eV. Transmission electron microscopy (TEM) image was obtained on a microscope (200 kV, Tecnai G2 F20, FEI, United States). Electron paramagnetic resonance (EPR) spectra were acquired on a spectrometer (E500, Bruker, United States) under the X-band microwave (9.433 GHz, 0.998 mW) at 298 K with modulation frequency of 100 kHz, in which 2,2-Diphenyl-1-picrylhydrazyl (DPPH) was used as standard sample to analyze spin concentration. The N_2 adsorption-desorption isotherms at 77 K were investigated on an analyzer (3Flex, Micromeritics, United States). The specific surface areas (SSAs) were analyzed via the Brunauer–Emmett–Teller (BET) method. Inductively coupled plasma-optical emission spectrometry (ICP-OES, Agilent ICP-OES 720, United States) was performed to determine the presence of Cl residues.

2.3 Electrochemical measurements

A three-electrode configuration and CHI760E electrochemical workstation were used to evaluate HER and OER activity in 1 M KOH (pH ≈ 14). The three electrodes include Ag/AgCl electrode with saturated KCl as reference electrode, carbon rod as counter electrode, and glassy carbon electrode (GCE) as working electrode that is connected to a rotating disk electrode (RDE) apparatus. Before preparing a GCE, a homogeneous dispersion of a sample including $NiCo_2O_4$-*n*KCl, 20wt% Pt/C or IrO_2, was first prepared as follows: 2.5 mg of a sample, 2.5 mg of carbon black and 50 µL of Nafion solution were added into 1 ml of absolute ethanol, and the mixture was treated by sonication for 30 min. Then, ~12.7 µL of the above dispersion was casted on the GCE with a diameter of 4 mm. After natural dried overnight, the GCE with a loading of ~0.24 mg cm^{-2} was obtained. According to the Nernst equation E (vs. RHE) = E (vs. Ag/AgCl) + 0.197 + 0.0591 × pH, the actual electrode potential relative to Ag/AgCl is converted to that relative to RHE.

Before the test, cyclic voltammetry (CV) was performed at a scanning rate of 50 mV s^{-1} until the curve is stable. The linear sweep voltammetry (LSV) at a scan rate of 5 mV s^{-1} was used to record the polarization curve of a sample. The durability of HER (OER) activity was studied by the chronopotentiometry of 30000 s at a constant HER (OER) current density of 10 mA cm^{-2}.

The electrochemically active surface area (EASA) is proportional to the electric double layer capacitance (C_{DL}) of an electrocatalyst. Therefore, the C_{DL} can be used to indirectly indicate the electrochemical active area of a catalyst. First, the CV curve was collected with a sweep rate of 10–50 mV s^{-1} within the potential window without Faradic currents. Subsequently, the difference between cathode and anode current density ($j = j_c$-j_a)

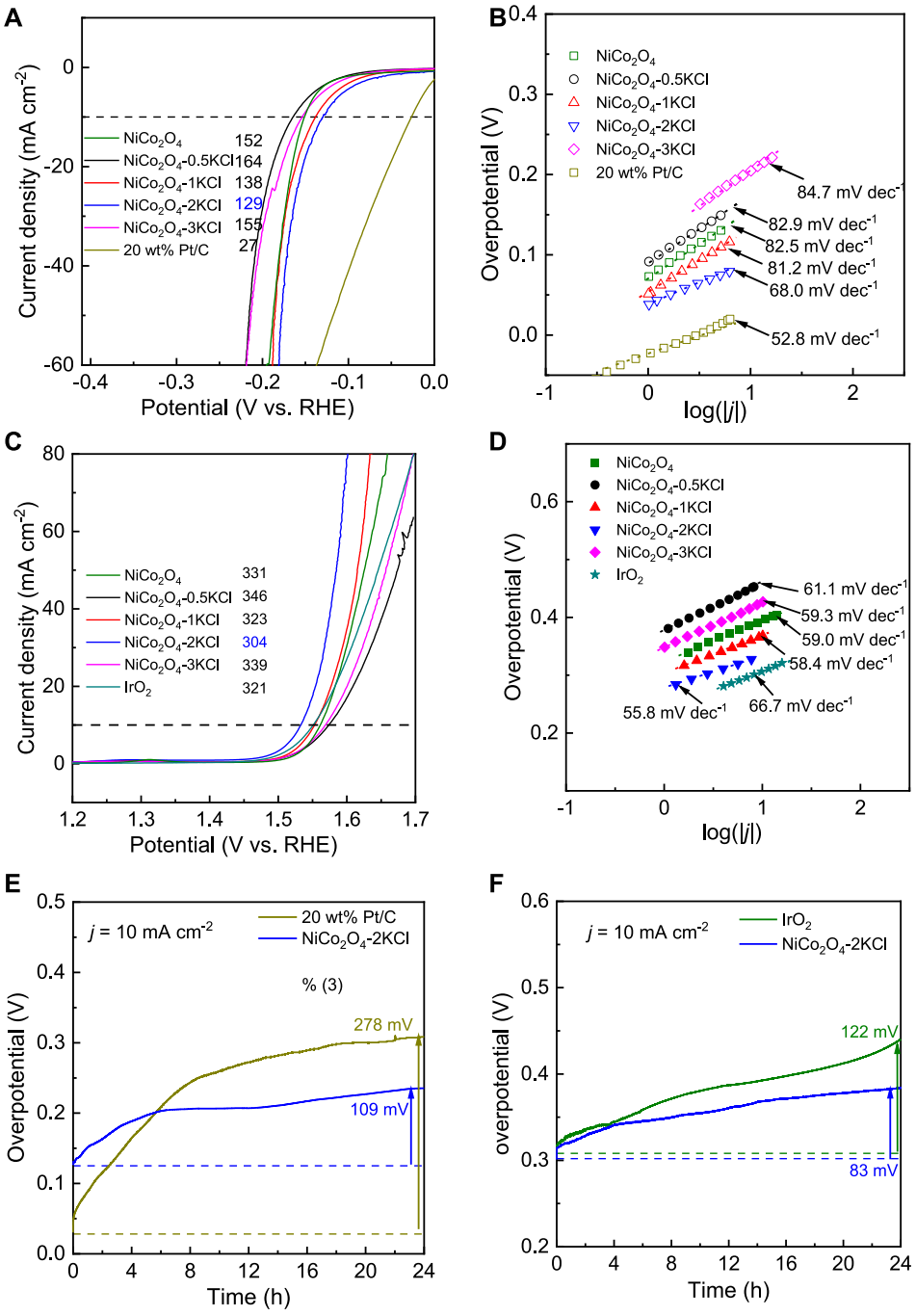

FIGURE 2
HER/OER activity and durability in 1 M KOH: **(A)** HER LSV curves; **(B)** HER Tafel plots; **(C)** OER LSV curves; **(D)** OER Tafel plots; **(E)** HER chronopotentiometry curves of 20 wt% Pt/C and $NiCo_2O_4$-2KCl at 10 mA cm^{-2}; **(F)** OER chronopotentiometry curves of IrO_2 and $NiCo_2O_4$-2KCl at 10 mA cm^{-2}.

was plotted as a function of sweep speeds (ν), and the C_{DL} is the half of the slope of this linear plot. Electrochemical impedance spectroscopy (EIS) is obtained at an AC frequency of 10^6–10^{-1} Hz under an open circuit voltage.

$NiCo_2O_4$-2KCl with the optimal bifunctional HER/OER activity was used as both cathode and anode catalysts in a symmetrical cell to test the overall water splitting performance, i.e., $NiCo_2O_4$-2KCl (cathode) ||$NiCo_2O_4$-2KCl

(anode). Hydrophobic carbon papers (0.5 × 0.5 cm^2) were used as working electrodes with the catalyst loading of ~0.24 mg cm^{-2} in both electrodes. In 1 M KOH, a LSV is performed within the potential range of 1.4–1.9 V at 5 mV s^{-1}. As a comparison, under the similar conditions, the performance of a water splitting cell with 20wt% Pt/C and IrO_2 as the cathode and anode catalysts (20wt% Pt/C||IrO_2), respectively, was also evaluated.

3 Results and discussion

3.1 Electrochemical catalytic performance

During the similar preparations, a series of $NiCo_2O_4$ samples were first prepared under the assistance of different salts, including KCl, KBr, KI, K_2SO_4 and KNO_3, in order to screening the optimal salt. Supplementary Figures S1A,B show the corresponding HER and OER LSV curves in 1 M KOH. As shown in Supplementary Figure S1C, $NiCo_2O_4$-2KCl shows the lowest overpotentials at 10 mA cm^{-2} toward both HER and OER, which demonstrates that the assisting effects of KCl on promoting HER and OER activity are better than the other salts. Thus, the assisting effects of different fed amounts of KCl were further evaluated. Figure 2A shows the HER LSV curves of $NiCo_2O_4$-*n*KCl and $NiCo_2O_4$. $NiCo_2O_4$ (without the assistance of KCl) needs an overpotential ($\eta_{10\text{-HER}}$) of ~152 mV to reach 10 mA cm^{-2}. However, the $\eta_{10\text{-HER}}$ of $NiCo_2O_4$-0.5KCl is slightly increased to ~164 mV relative to $NiCo_2O_4$. After further increasing the fed amount of KCl, the $\eta_{10\text{-HER}}$ decreases and subsequently increases. In other word, $NiCo_2O_4$-2KCl has the smallest $\eta_{10\text{-HER}}$ (~129 mV), though the $\eta_{10\text{-HER}}$ is still higher than that of 20wt% Pt/C (~27 mV). Figure 2B exhibits the corresponding HER Tafel plots. The Tafel slopes show a change trend similar to that of $\eta_{10\text{-HER}}$ values. Although the Tafel slope of $NiCo_2O_4$-2KCl (~68 mV dec^{-1}) is higher than that of 20 wt% Pt/C (~52.8 mV dec^{-1}), it is still the lowest one among the prepared $NiCo_2O_4$-*n*KCl samples, also lower that of $NiCo_2O_4$ (~82.5 mV dec^{-1}). It indicates the faster HER kinetic as compared with other samples, following Heyrovsky and Tafel reactions as rate-determining steps (Zhang et al., 2018a). In addition, the OER LSV curves are shown in Figure 2C. The change trend of the OER overpotential ($\eta_{10\text{-OER}}$) along with the fed amounts of KCl is similar to that for $\eta_{10\text{-HER}}$ (Figure 2A). Similar to the HER activity, $NiCo_2O_4$-2KCl has the lowest $\eta_{10\text{-OER}}$ (~304 mV) among the prepared samples, which is lower than that of IrO_2 (~321 mV). Figure 2D exhibits the corresponding OER Tafel plots. $NiCo_2O_4$-2KCl has the lowest Tafel slope of ~55.8 mV dec^{-1}, also lower than that of IrO_2 (~66.7 mV dec^{-1}), indicating the highest OER kinetics among the prepared samples. The above results demonstrate that the fed amount of KCl significantly affects the HER and OER activity of $NiCo_2O_4$ samples, and a moderate amount of KCl is required to optimize both HER and OER activity. Table 1 shows the summary of HER and OER activity of some typical electrocatalysts reported in the literatures. Obviously, the HER and OER catalytic performance of $NiCo_2O_4$-2KCl is comparable to that of the recently-developed HER/OER bifunctional catalysts, although the highly conductive substrates were not applied to support as the binder-free electrodes, such as carbon cloth (Dong et al., 2022), Ni foams (Ha et al., 2019; Du et al., 2021; He et al., 2021), etc.

According to the above discussion, $NiCo_2O_4$-2KCl with the moderate amount of KCl ($n = 2$) assisted has the optimized HER and OER activity. Further, chronopotentiometry in 1 M KOH was used to evaluate the durability of HER and OER activity of $NiCo_2O_4$-2KCl plus noble metal benchmarked samples (i.e., 20wt% Pt/C as HER benchmarked catalyst and IrO_2 as OER benchmarked catalyst). As shown in Figure 2E, the $\Delta\eta_{10\text{-HER}}$ of 20 wt% Pt/C is high up to ~278 mV after a running of 24 h, while the $\Delta\eta_{10\text{-HER}}$ of $NiCo_2O_4$-2KCl is only ~109 mV. As shown in Figure 2F, the $\Delta\eta_{10\text{-OER}}$ of IrO_2 and $NiCo_2O_4$-2KCl are ~122 and ~83 mV, respectively, when the running time of OER processes at 10 mA cm^{-2} is 24 h, showing the lower $\Delta\eta_{10\text{-OER}}$ of $NiCo_2O_4$-2KCl. The evaluation results clearly shows that $NiCo_2O_4$-2KCl has the excellent HER and OER durability, and has the potential as a bifunctional overall water splitting catalyst.

In view of the excellent HER and OER activity and durability of $NiCo_2O_4$-2KCl, it was used as both cathode and anode catalyst for a water splitting cell. For comparison, 20 wt% Pt/C (cathode, HER)||IrO_2 (anode, OER) cell was also used for water splitting. Figure 3A shows the LSV curves of water splitting of the 2 cells. 20 wt% Pt/C||IrO_2 needs ~1.63 V to drive a current density of 10 mA cm^{-2}, while $NiCo_2O_4$-2KCl||$NiCo_2O_4$-2KCl requires a slightly higher voltage of ~1.66 V to achieve 10 mA cm^{-2}. In addition, when the voltage exceeds 1.73 V, the overall water splitting current density of $NiCo_2O_4$-2KCl||$NiCo_2O_4$-2KCl is higher than that of 20 wt% Pt/C||IrO_2. It suggests that the overall water splitting performance of $NiCo_2O_4$-2KCl||$NiCo_2O_4$-2KCl is comparable to that of 20 wt% Pt/C||IrO_2 and other cells (Table 1). Furthermore, as shown in Figure 3B, $NiCo_2O_4$-2KCl||$NiCo_2O_4$-2KCl can run stably for 240 h at ~1.66 V with the higher current retention of ~88% as compared with the 20 wt% Pt/C||IrO_2 (~84% at 1.63 V) that also runs for 240 h.

All in all, $NiCo_2O_4$-2KCl, which is prepared by the assistance of KCl with the moderate fed amounts, affords the optimal HER, OER and overall water splitting catalytic performance.

3.2 Structural features

Figure 4A shows the XRD patterns of $NiCo_2O_4$ without the assistance of KCl and $NiCo_2O_4$-2KCl. All the diffraction peaks are consistent with the ones of PDF# 73-1702, which are all attributed to $NiCo_2O_4$ with inverse spinel structure. Generally,

TABLE 1 The summary of HER and OER activity and overall water splitting performance of the recently reported catalysts in 1 M KOH.

Catalysts	Substrates	η_{10-HER} (mV)	η_{10-OER} (mV)	Overall water splitting voltage @ 10 mA cm^{-2} (V)	References
$NiCo_2O_4$-2KCl	**GCE (binder)[a]**	**129**	**304**	**1.66**	**This work**
FeOOH@$NiCo_2O_4$	Ni foil (binder)	146	203	1.58	Cao et al. (2020)
Amorphous Ni-Co-S nanoflake arrays	Carbon cloth (binder-free)[b]	192	296	1.60	Dong et al. (2022)
Co_9S_8@$NiCo_2O_4$	Ni foam (binder-free)	104	270@100 mA cm^{-2}	1.55	Du et al. (2021)
N-$NiCo_2O_4$@C	Ni foam (binder-free)	42	242	1.43	Ha et al. (2019)
FeP-NCO	Ni foam (binder-free)	82	220	1.523	He et al. (2021)
$NiCo_2O_4$ hollow microcuboids	Ni foam (binder)	110 in 1 M NaOH	290 in 1 M NaOH	1.65	Gao et al. (2016)
$NiCo_2O_4$/Cu_xO	Cu foam (binder-free)	92	213	1.61	Ouyang et al. (2021)
Cobalt phosphide/N-doped carbon nanotubes	GCE (binder)	94	317	1.619	Yang et al. (2021)
CoP@FeCoP/N-doped carbon	Carbon paper (binder)	141	238	1.68	Shi et al. (2021)
NiCoP nanorod array	Ni foam (binder-free)	60	153	1.55	Hu et al. (2021)
Co-Mo_2C@N-doped carbon	GCE (binder)	92	338	1.68	Zhang et al. (2021)

[a]"Binder" represents that the preparation of an electrode needs polymer binders to bind powder-like catalysts on the surface of the electrode.
[b]"Binder-free" means that the target catalyst has grown directly on the used substrate to form a self-supported electrode.

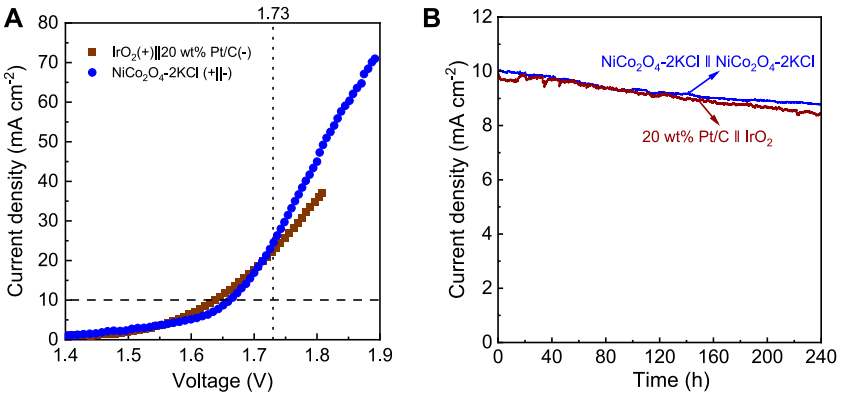

FIGURE 3
(A) LSV curves of overall water splitting in 1 M KOH for $NiCo_2O_4$-2KCl|| $NiCo_2O_4$-2KCl and 20 wt% Pt/C||IrO_2 cells; **(B)** *I*-t curves of $NiCo_2O_4$-2KCl|| $NiCo_2O_4$-2KCl (at ~1.66 V) and 20 wt% Pt/C||IrO_2 cells (at ~1.63 V) for 240 h.

the narrower the full width at half maxima (FWHM) of diffraction peaks, the larger the grain size. According to the Scherer equation $D = (K\times\gamma)/(B\times\cos\theta)$, in which D is the average grain size, K is the Scherrer constant, γ is wavelength of X-ray, B is FWHM of diffraction peaks, and θ is the half of Bragg angle, the average grain sizes of $NiCo_2O_4$ and $NiCo_2O_4$-2KCl can be estimated. Thus, the mean grain size of $NiCo_2O_4$ is larger (~93 nm) and the crystallinity is high. By contrast, the diffraction peak intensities of $NiCo_2O_4$-2KCl are obviously weakened, and the FWHM is obviously broadened, which indicates that its crystallinity has decreased and the average grain size has become much smaller (~35 nm). It suggests that the used KCl significantly limits the growth of $NiCo_2O_4$ nanoparticles.

Figure 4B shows the XPS Ni 2p spectra of $NiCo_2O_4$ and $NiCo_2O_4$-2KCl. For both $NiCo_2O_4$ and $NiCo_2O_4$-2KCl, only the peaks attributed to Ni^{2+} are deconvoluted and located at ~855.8 eV (Bao et al., 2021), while the broad ones at ~861.6 eV are ascribed to the satellite peaks, which suggests that the chemical states of Ni^{2+} are similar in them. As shown in Figure 4C, $NiCo_2O_4$-2KCl has more O_v and thus the higher O_v/O^{2-} (lattice oxygen) molar ratio of ~0.81 as compared with

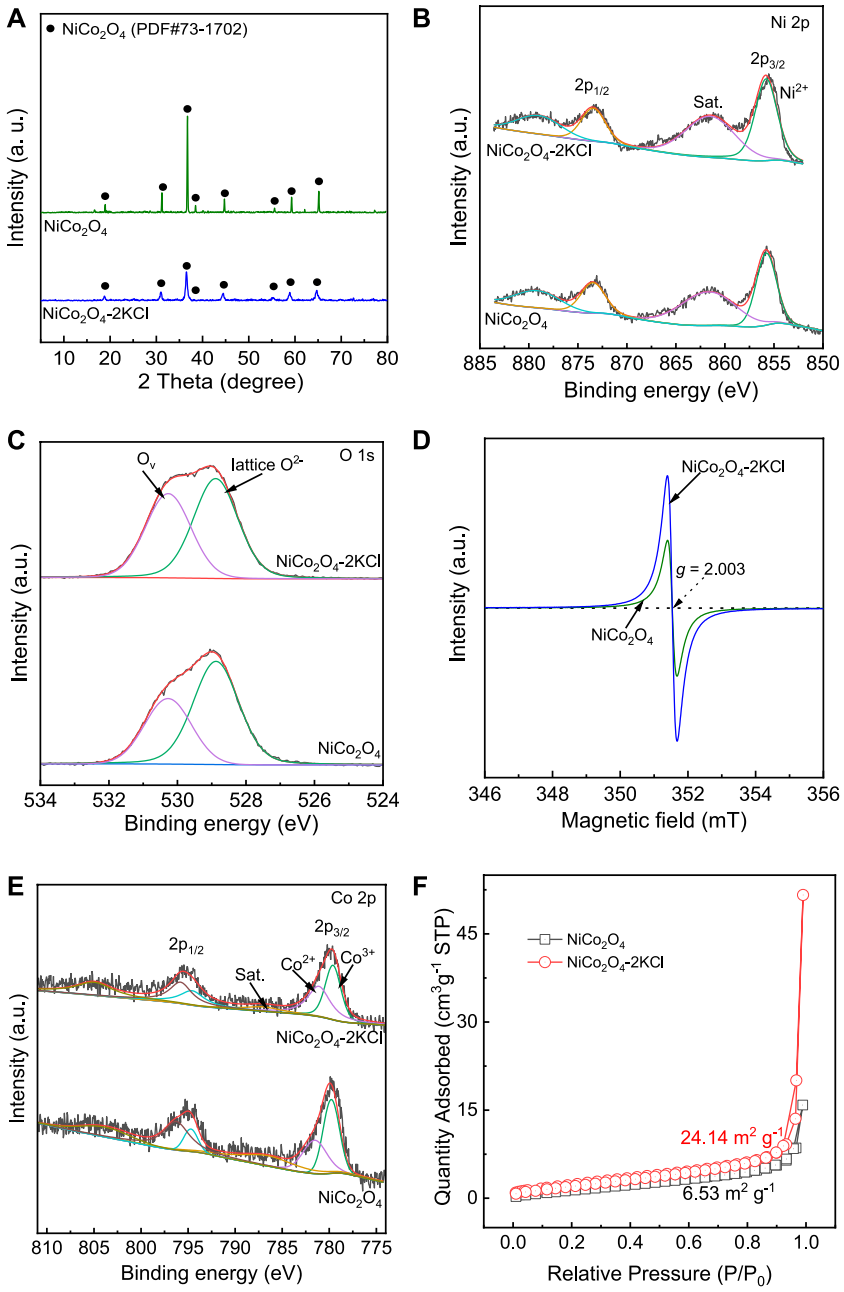

FIGURE 4
Structural characterizations of $NiCo_2O_4$ and $NiCo_2O_4$-2KCl: **(A)** XRD patterns; **(B)** XPS Ni 2p spectra; **(C)** XPS O 1s spectra; **(D)** EPR spectra; **(E)** XPS Co 2p spectra; **(F)** N_2 adsorption-desorption isotherms at 77 K.

$NiCo_2O_4$ (~0.59 of O_v/O^{2-} molar ratio). The EPR spectra (Figures 4D, Supplementary Figure S2) with *g*-factor of ~2.003 that is close to that of free electrons further confirm that all samples have more or less O_v. The samples with the assistance of KCl except $NiCo_2O_4$-0.5KCl (~1.67×10^{14} spins g^{-1}) are generally richer in O_v with the higher spin concentration (~7.68×10^{14} spins g^{-1} for $NiCo_2O_4$-2KCl, ~5.67×10^{14} spins g^{-1} for $NiCo_2O_4$-1KCl, ~4.84×10^{14} spins g^{-1} for $NiCo_2O_4$-3KCl) as compared with $NiCo_2O_4$ (~3.89×10^{14} spins g^{-1}) without the assistance of KCl, due to the ability of more O_v to capture more unpaired electrons (Kaftelen et al., 2012; Chen et al., 2021). Obviously, the more O_v formed in $NiCo_2O_4$-*n*KCl is closely related with the assistance of KCl during the preparations. To balance charge distribution, some parts of Co^{3+} at ~779.7 eV are reduced to Co^{2+}

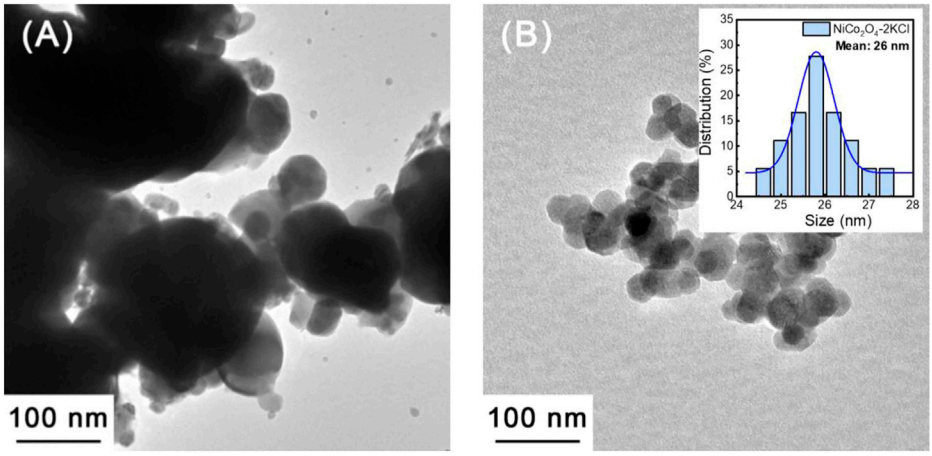

FIGURE 5
TEM images: **(A)** $NiCo_2O_4$ and **(B)** $NiCo_2O_4$-2KCl.

(Yan et al., 2018), which is indicated by Co 2p spectra (Figure 4E). Although there is additional Co^{2+} in both $NiCo_2O_4$ and $NiCo_2O_4$-2KCl, on one hand, the binding energy of Co^{2+} in $NiCo_2O_4$-2KCl (~781.1 eV) is lower than that in $NiCo_2O_4$ (~781.5 eV); on the other hand, the Co^{2+}/Co^{3+} molar ratio in $NiCo_2O_4$-2KCl (~1.00) is higher than that in $NiCo_2O_4$ (~0.72). The results of Co 2p spectra suggest that the relatively more Co^{3+} is reduced to Co^{2+} in $NiCo_2O_4$-2KCl as compared with $NiCo_2O_4$.

The N_2 adsorption-desorption isotherms at 77 K of $NiCo_2O_4$-2KCl and $NiCo_2O_4$ are shown in Figure 4F. The corresponding BET SSA of $NiCo_2O_4$-2KCl is ~24.14 $m^2\ g^{-1}$, which is ~3.7 times of that of $NiCo_2O_4$ (~6.53 $m^2\ g^{-1}$). Thus, KCl play an important role in achieving the higher SSA for $NiCo_2O_4$ during the preparations, which is consistent with the average grain sizes of them determined by Scherer equation.

Figure 5A shows the TEM image of $NiCo_2O_4$ synthesized without the assistance of KCl. Obviously, the size distribution of $NiCo_2O_4$ particles is uneven. Quite large and very small particles coexist in this sample. The mean grain size of $NiCo_2O_4$ can be referred to the XRD results (~93 nm). In comparison with $NiCo_2O_4$, $NiCo_2O_4$-2KCl has a smaller mean particle size (~26 nm in inset of Figure 5B), and the size distribution is relatively narrower and more uniform. The results of TEM indicate that the KCl does effectively reduce the mean sizes of $NiCo_2O_4$ nanoparticles, which is consistent with the XRD results. In addition, as shown in Supplementary Figure S3, the unwashed intermediate after annealed contains KCl and $NiCo_2O_4$ nanoparticles, and KCl nanoparticles combine with $NiCo_2O_4$ nanoparticles tightly, thus playing the role in inhibiting the growth of $NiCo_2O_4$ nanoparticles.

3.3 Further brief discussion on catalytic performance

The CV curves within the potential window without Faradic currents were used to determine C_{DL}, because C_{DL} is proportional to the EASA of a catalyst (Gao et al., 2020; Wang et al., 2020). The corresponding CV curves are shown in Supplementary Figure S4, and the linear relationship between the difference of cathode and anode current density ($j = j_c$-j_a) and scan rate is shown in Figure 6A. With the increase of n, the C_{DL} values obtained from the half of the slopes of the linear plots show a trend similar to that for the HER or OER activity. Among $NiCo_2O_4$ and the $NiCo_2O_4$-nKCl samples, the C_{DL} of $NiCo_2O_4$-2KCl is largest, as high as ~13.72 mF cm^{-2} Figure 6B shows the EIS spectra of $NiCo_2O_4$ and the $NiCo_2O_4$-nKCl samples. The charge transfer resistance (R_{ct}) value of $NiCo_2O_4$-2KCl is lowered to 7.54 ohm, indicating the faster charge transfer between the GCE loaded with it and the electrolyte during the electrocatalysis as compared with the other samples.

As the ICP-OES results shown, there is no Cl residues detected within the detection limits of the used analyzer after three tests of every samples. Hence, KCl plays the indirect but important roles in electrocatalytic performance. According to the above results, KCl has great influences on the structures and surface compositions of $NiCo_2O_4$. The XRD and TEM results demonstrate that the average size of $NiCo_2O_4$-2KCl nanoparticles is significantly smaller than that of $NiCo_2O_4$. This indicates that KCl restricts the growth of $NiCo_2O_4$ nanoparticles. The smaller size of $NiCo_2O_4$-2KCl nanoparticles is favorable to exposing more active sites. In addition, the amount of O_v in $NiCo_2O_4$-2KCl is significantly increased as compared with $NiCo_2O_4$. Some studies have shown

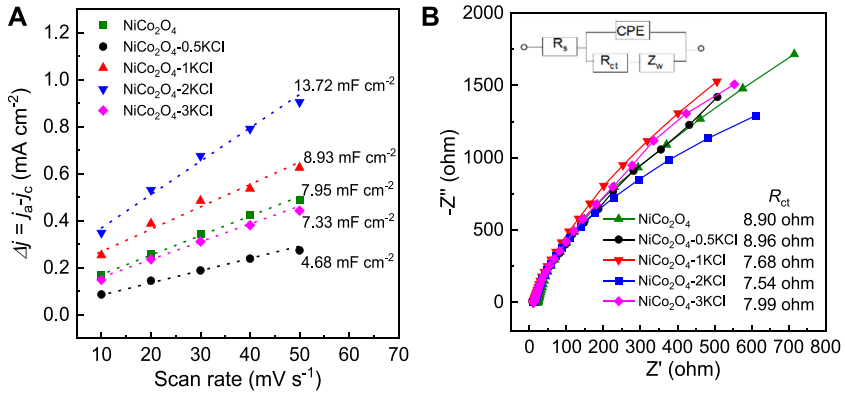

FIGURE 6
(A) The relationship between Δj (= j_a-j_c) and scan rate; **(B)** EIS spectra at open circuit voltage, and the inset is the corresponding equivalent circuit.

that oxides are more likely to form O_v under confinement effects (Kotomin et al., 2011; Arrigoni et al., 2016; Ye et al., 2022), and the generation energy of O_v in a small space becomes lower. Herein, KCl particles can limit the growth of $NiCo_2O_4$ nanoparticles due to the tight integration with each other (Supplementary Figure S3). When $NiCo_2O_4$ is gradually formed during annealing, a large number of O_v will be generated. Many studies have shown that O_v has been proven to exert favorable roles in promoting HER (Zhang et al., 2018b; Li et al., 2021b; Lu et al., 2021) and OER (Liu et al., 2019; Xiao et al., 2020; Zhong et al., 2021) activity in alkaline conditions, mainly because the O_v lowers the coordination numbers of active metal ions, and thus modifies their electronic structures and further tunes the adsorption strength of HER and OER intermediates (*H for HER, and *OH, *O and *OOH for OER) on them and the O_v also can decrease the energy barriers during HER or OER processes (Zhu et al., 2020b; Badreldin et al., 2021; Wu et al., 2021). Together plus the effects of the smaller sizes, $NiCo_2O_4$-2KCl with the more O_v can expose more active sites on its surface and achieves the higher EASAs (Figure 6A) as compared with $NiCo_2O_4$. In addition to favorable contributions to active sites, O_v can efficiently capture unpaired electrons and form additional energy levels in the band gap of $NiCo_2O_4$ samples, thus increasing the concentration of carriers and enhancing the charge transfer efficiency during electrochemical processes (Shin et al., 2020; Badreldin et al., 2021), which is indicated by the corresponding EIS spectra (Figure 6B) and the relationship between spin concentrations (proportional to the contents of O_v) and R_{ct} values (Supplementary Figure S5). The higher charge transfer efficiency is more conducive to make full use of the exposed active sites and thus the activity of HER and OER. In summary, for $NiCo_2O_4$-2KCl, the small size and abundant O_v provide significant roles on promoting HER and OER with high bifunctional catalytic activity.

4 Conclusion

In this work, a salt-assisted method was used to prepare small-sized $NiCo_2O_4$ with abundant O_v as highly active catalyst for HER, OER and overall water splitting. KCl is used as a good agent to limit the growth of $NiCo_2O_4$ nanoparticles. The confinement effects resulted from KCl during the calcination processes effectively increases the amount of O_v in $NiCo_2O_4$ nanoparticles, thereby increasing the densities of active sites and enhancing charge transfer efficiency. As compared with $NiCo_2O_4$ without the assistance of KCl, both the reduced nanoparticle size and the more O_v are favorable for the optimal $NiCo_2O_4$-2KCl to expose more active sites and increase the EASA. As a result, the optimal $NiCo_2O_4$-2KCl exhibits the higher bifunctional catalytic activity of both HER and OER than $NiCo_2O_4$ and the other $NiCo_2O_4$-*n*KCl samples. When $NiCo_2O_4$-2KCl is used as both cathode and anode for overall water splitting, it can drive $NiCo_2O_4$-2KCl||$NiCo_2O_4$-2KCl cell to have the similar performance to that of 20 wt% Pt/C||IrO_2 cell. This work provides an efficient method to prepare highly active catalyst toward electrocatalytic water splitting to hydrogen.

Data availability statement

The original contributions presented in the study are included in the article/Supplementary Material, further inquiries can be directed to the corresponding author.

Author contributions

XH, YD, and FY contributed to conception and design of the study. FY supervised the study. XH, YD, XZ, and GL performed the experiments. XH and YD analyzed the results. XH and YD wrote the first draft of the manuscript. All authors contributed to manuscript revision, read, and approved the submitted version.

Funding

This work is supported by the National Natural Science Foundation of China (22078027) and International Joint Lab of Jiangsu Education Department. Special thanks to the support from Advanced Catalysis and Green Manufacturing Collaborative Innovation Center, Changzhou University (ACGM2016-06-02 and ACGM2016-06-03), A Project Funded by the Priority Academic Program Development of Jiangsu Higher Education Institutions (PAPD) and Postgraduate Research & Practice Innovation Program of Jiangsu Province.

Conflict of interest

The authors declare that the research was conducted in the absence of any commercial or financial relationships that could be construed as a potential conflict of interest.

Publisher's note

All claims expressed in this article are solely those of the authors and do not necessarily represent those of their affiliated organizations, or those of the publisher, the editors and the reviewers. Any product that may be evaluated in this article, or claim that may be made by its manufacturer, is not guaranteed or endorsed by the publisher.

Supplementary material

The Supplementary Material for this article can be found online at: https://www.frontiersin.org/articles/10.3389/fchem.2022.996084/full#supplementary-material

References

Arrigoni, M., Bjørheim, T. S., Kotomin, E., and Maier, J. (2016). First principles study of confinement effects for oxygen vacancies in $BaZrO_3$ (001) ultra-thin films. *Phys. Chem. Chem. Phys.* 18, 9902–9908. doi:10.1039/c6cp00830e

Badreldin, A., Abusrafa, A. E., and Abdel-Wahab, A. (2021). Oxygen-deficient cobalt-based oxides for electrocatalytic water splitting. *ChemSusChem* 14, 10–32. doi:10.1002/cssc.202002002

Bao, W., Xiao, L., Zhang, J., Jiang, P., Zou, X., Yang, C., et al. (2021). Electronic and structural engineering of $NiCo_2O_4$/Ti electrocatalysts for efficient oxygen evolution reaction. *Int. J. Hydrogen Energy* 46, 10259–10267. doi:10.1016/j.ijhydene.2020.12.126

Cao, X., Sang, Y., Wang, L., Ding, G., Yu, R., and Geng, B. (2020). A multi-interfacial FeOOH@$NiCo_2O_4$ heterojunction as a highly efficient bifunctional electrocatalyst for overall water splitting. *Nanoscale* 12, 19404–19412. doi:10.1039/d0nr05216g

Chen, B., Jiang, Z., Huang, J., Deng, B., Zhou, L., Jiang, Z-J., et al. (2018). Cation exchange synthesis of $Ni_xCo_{(3-x)}O_4$ (x= 1.25) nanoparticles on aminated carbon nanotubes with high catalytic bifunctionality for the oxygen reduction/evolution reaction toward efficient Zn-air batteries. *J. Mat. Chem. A Mat.* 6, 9517–9527. doi:10.1039/c8ta01177j

Chen, S., Huang, D., Liu, D., Sun, H., Yan, W., Wang, J., et al. (2021). Hollow and porous $NiCo_2O_4$ nanospheres for enhanced methanol oxidation reaction and oxygen reduction reaction by oxygen vacancies engineering. *Appl. Catal. B Environ.* 291, 120065. doi:10.1016/j.apcatb.2021.120065

Dawood, F., Anda, M., and Shafiullah, G. M. (2020). Hydrogen production for energy: An overview. *Int. J. Hydrogen Energy* 45, 3847–3869. doi:10.1016/j.ijhydene.2019.12.059

Dong, Y., Fang, Z., Yang, W., Tang, B., and Liu, Q. (2022). Integrated bifunctional electrodes based on amorphous Co-Ni-S nanoflake arrays with atomic dispersity of active sites for overall water splitting. *ACS Appl. Mat. Interfaces* 14, 10277–10287. doi:10.1021/acsami.1c22092

Du, X., Zhang, C., Wang, H., Wang, Y., and Zhang, X. (2021). Controlled synthesis of Co_9S_8@$NiCo_2O_4$ nanorod arrays as binder-free electrodes for water splitting with impressive performance. *J. Alloys Compd.* 885, 160972. doi:10.1016/j.jallcom.2021.160972

Gao, X., Wang, P., Pan, Z., Claverie, J. P., and Wang, J. (2020). Recent progress in two-dimensional layered double hydroxides and their derivatives for supercapacitors. *ChemSusChem* 13, 1226–1254. doi:10.1002/cssc.201902753

Gao, X., Zhang, H., Li, Q., Yu, X., Hong, Z., Zhang, X., et al. (2016). Hierarchical $NiCo_2O_4$ hollow microcuboids as bifunctional electrocatalysts for overall water-splitting. *Angew. Chem. Int. Ed. Engl.* 55, 6398–6402. doi:10.1002/ange.201600525

Ha, Y., Shi, L., Yan, X., Chen, Z., Li, Y., Xu, W., et al. (2019). Multifunctional electrocatalysis on a porous N-doped $NiCo_2O_4$@ C nanonetwork. *ACS Appl. Mat. Interfaces* 11, 45546–45553. doi:10.1021/acsami.9b13580

He, B., Pan, G., Deng, Y., Zhao, L., Wang, H., Wang, R., et al. (2021). Hierarchical iron-phosphide@ $NiCo_2O_4$ nanoneedle arrays for high performance water splitting. *Appl. Surf. Sci.* 569, 151016. doi:10.1016/j.apsusc.2021.151016

Hjeij, D., Bicer, Y., and Koc, M. (2022). Hydrogen strategy as an energy transition and economic transformation avenue for natural gas exporting countries: Qatar as a case study. *Int. J. Hydrogen Energy* 47, 4977–5009. doi:10.1016/j.ijhydene.2021.11.151

Hu, H-S., Li, Y., Shao, Y-R., Li, K-X., Deng, G., Wang, C-B., et al. (2021). NiCoP nanorod arrays as high-performance bifunctional electrocatalyst for overall water splitting at high current densities. *J. Power Sources* 484, 229269. doi:10.1016/j.jpowsour.2020.229269

Jung, H., Ma, A., Abbas, S. A., Kim, H. Y., Choe, H. R., Jo, S. Y., et al. (2021). A new synthetic approach to cobalt oxides: Designed phase transformation for electrochemical water splitting. *Chem. Eng. J.* 415, 127958. doi:10.1016/j.cej.2020.127958

Kaftelen, H., Ocakoglu, K., Thomann, R., Tu, S., Weber, S., and Erdem, E. (2012). EPR and photoluminescence spectroscopy studies on the defect structure of ZnO nanocrystals. *Phys. Rev. B* 86, 014113. doi:10.1103/physrevb.86.014113

Kim, M., Park, J., Wang, M., Wang, Q., Kim, M. J., Kim, J. Y., et al. (2022). Role of surface steps in activation of surface oxygen sites on Ir nanocrystals for oxygen evolution reaction in acidic media. *Appl. Catal. B Environ.* 302, 120834. doi:10.1016/j.apcatb.2021.120834

Kotomin, E. A., Alexandrov, V., Gryaznov, D., Evarestov, R. A., and Maier, J. (2011). Confinement effects for ionic carriers in $SrTiO_3$ ultrathin films: First-principles calculations of oxygen vacancies. *Phys. Chem. Chem. Phys.* 13, 923–926. doi:10.1039/c0cp01060j

Lee, J. E., Shafiq, I., Hussain, M., Lam, S. S., Rhee, G. H., and Park, Y-K. (2022). A review on integrated thermochemical hydrogen production from water. *Int. J. Hydrogen Energy* 47, 4346–4356. doi:10.1016/j.ijhydene.2021.11.065

Li, C., Zhou, E., Yu, Z., Liu, H., and Xiong, M. (2020). Tailor-made open porous 2D CoFe/SN-carbon with slightly weakened adsorption strength of ORR/OER

intermediates as remarkable electrocatalysts toward zinc-air batteries. *Appl. Catal. B Environ.* 269, 118771. doi:10.1016/j.apcatb.2020.118771

Li, P., Wang, H., Fan, W., Huang, M., Shi, J., Shi, Z., et al. (2021). Salt assisted fabrication of lignin-derived Fe, N, P, S codoped porous carbon as trifunctional catalyst for Zn-air batteries and water-splitting devices. *Chem. Eng. J.* 421, 129704. doi:10.1016/j.cej.2021.129704

Li, Z., Yang, Y., Wang, S., Gu, L., and Shao, S. (2021). High-density ruthenium single atoms anchored on oxygen-vacancy-rich g-C_3N_4-C-TiO_2 heterostructural nanosphere for efficient electrocatalytic hydrogen evolution reaction. *ACS Appl. Mat. Interfaces* 13, 46608–46619. doi:10.1021/acsami.1c12494

Liu, Y., Liu, P., Qin, W., Wu, X., and Yang, G. (2019). Laser modification-induced $NiCo_2O_{4-\delta}$ with high exterior Ni^{3+}/Ni^{2+} ratio and substantial oxygen vacancies for electrocatalysis. *Electrochim. Acta* 297, 623–632. doi:10.1016/j.electacta.2018.11.111

Lu, J., Qian, G., Luo, L., He, H., and Yin, S. (2021). Contributions of oxygen vacancies to the hydrogen evolution catalytic activity of tungsten oxides. *Int. J. Hydrogen Energy* 46, 676–682. doi:10.1016/j.ijhydene.2020.09.229

Ouyang, Q., Lei, Z., Li, Q., Li, M., and Yang, C. (2021). A self-supported $NiCo_2O_4$/Cu_xO nanoforest with electronically modulated interfaces as an efficient electrocatalyst for overall water splitting. *J. Mat. Chem. A Mat.* 9, 14466–14476. doi:10.1039/d1ta00710f

Peng, C., Zhao, W., Li, Z., Kuang, Z., Cheng, G., Miller, J. T., et al. (2021). Eutectic molten salt assisted synthesis of highly defective and flexible ruthenium oxide for efficient overall water splitting. *Chem. Eng. J.* 425, 131707. doi:10.1016/j.cej.2021.131707

Ranjani, M., Senthilkumar, N., and Manthiram, A. (2018). 3D flower-like hierarchical $NiCo_2O_4$ architecture on carbon cloth fibers as an anode catalyst for high-performance, durable direct urea fuel cells. *J. Mat. Chem. A Mat.* 6, 23019–23027. doi:10.1039/c8ta08405j

Shi, J., Qiu, F., Yuan, W., Guo, M., and Lu, Z. H. (2021). Nitrogen-doped carbon-decorated yolk-shell CoP@FeCoP micro-polyhedra derived from MOF for efficient overall water splitting. *Chem. Eng. J.* 403, 126312. doi:10.1016/j.cej.2020.126312

Shin, Y., Doh, K-Y., Kim, S. H., Lee, J. H., Bae, H., Song, S-J., et al. (2020). Effect of oxygen vacancies on electrical conductivity of $La_{0.5}Sr_{0.5}FeO_{3-\delta}$ from first-principles calculations. *J. Mat. Chem. A Mat.* 8, 4784–4789. doi:10.1039/c9ta12734h

Sun, B., Miao, F., Tao, B., Wang, Y., Zang, Y., and Chu, P. K. (2021). Three-dimensional $NiCo_2O_4$ nanosheets and nanoflowers electrodeposited with palladium nanoparticles on nickel foam for the hydrogen evolution reaction. *J. Phys. Chem. Solids* 158, 110255. doi:10.1016/j.jpcs.2021.110255

Tenhumberg, N., and Büker, K. (2020). Ecological and economic evaluation of hydrogen production by different water electrolysis technologies. *Chem. Ing. Tech.* 92, 1586–1595. doi:10.1002/cite.202000090

Wang, J., He, Y., Yang, Q., Li, H., Xie, Z., Fan, Y., et al. (2019). Self-standing and efficient bifunctional electrocatalyst for overall water splitting under alkaline media enabled by $Mo_{1-x}Co_xS_2$ nanosheets anchored on carbon fiber paper. *Int. J. Hydrogen Energy* 44, 13205–13213. doi:10.1016/j.ijhydene.2019.03.161

Wang, P., Zhu, J., Pu, Z., Qin, R., Zhang, C., Chen, D., et al. (2021). Interfacial engineering of Co nanoparticles/Co_2C nanowires boosts overall water splitting kinetics. *Appl. Catal. B Environ.* 296, 120334. doi:10.1016/j.apcatb.2021.120334

Wang, Y., Ge, Z., Li, X., Zhao, J., Ma, B., and Chen, Y. (2020). Cu_2S nanorod arrays with coarse surfaces to enhance the electrochemically active surface area for water oxidation. *J. Colloid Interface Sci.* 567, 308–315. doi:10.1016/j.jcis.2020.02.030

Wu, Z., Zhao, Y., Jin, W., Jia, B., Wang, J., and Ma, T. (2021). Recent progress of vacancy engineering for electrochemical energy conversion related applications. *Adv. Funct. Mat.* 31, 2009070. doi:10.1002/adfm.202009070

Xiao, Y., Wang, Y., Xiao, M., Liu, C., Hou, S., Ge, J., et al. (2020). Regulating the pore structure and oxygen vacancies of cobaltosic oxide hollow dodecahedra for an enhanced oxygen evolution reaction. *NPG Asia Mat.* 12, 73. doi:10.1038/s41427-020-00255-y

Yan, D., Wang, W., Luo, X., Chen, C., Zeng, Y., and Zhu, Z. (2018). $NiCo_2O_4$ with oxygen vacancies as better performance electrode material for supercapacitor. *Chem. Eng. J.* 334, 864–872. doi:10.1016/j.cej.2017.10.128

Yang, D., Hou, W., Lu, Y., Zhang, W., and Chen, Y. (2021). Cobalt phosphide nanoparticles supported within network of N-doped carbon nanotubes as a multifunctional and scalable electrocatalyst for water splitting. *J. Energy Chem.* 52, 130–138. doi:10.1016/j.jechem.2020.04.005

Ye, J., Yang, D., Dai, J., Li, C., and Yan, Y. (2022). Confinement of ultrafine Co_3O_4 nanoparticles in nitrogen-doped graphene-supported macroscopic microspheres for ultrafast catalytic oxidation: Role of oxygen vacancy and ultrasmall size effect. *Sep. Purif. Technol.* 281, 119963. doi:10.1016/j.seppur.2021.119963

Yu, Z-Y., Duan, Y., Feng, X-Y., Yu, X., Gao, M-R., and Yu, S-H. (2021). Clean and affordable hydrogen fuel from alkaline water splitting: Past, recent progress, and future prospects. *Adv. Mat.* 33, 2007100. doi:10.1002/adma.202007100

Zhang, J., Wang, E., Cui, S., Yang, S., Zou, X., and Gong, Y. (2022). Single-atom Pt anchored on oxygen vacancy of monolayer $Ti_3C_2T_x$ for superior hydrogen evolution. *Nano Lett.* 22, 1398–1405. doi:10.1021/acs.nanolett.1c04809

Zhang, L., Jia, Y., Yan, X., and Yao, X. (2018). Activity origins in nanocarbons for the electrocatalytic hydrogen evolution reaction. *Small* 14, 1800235. doi:10.1002/smll.201800235

Zhang, P., Liu, Y., Liang, T., Ang, E. H., Zhang, X., Ma, F., et al. (2021). Nitrogen-doped carbon wrapped Co-Mo_2C dual Mott-Schottky nanosheets with large porosity for efficient water electrolysis. *Appl. Catal. B Environ.* 284, 119738. doi:10.1016/j.apcatb.2020.119738

Zhang, T., Wu, M-Y., Yan, D-Y., Mao, J., Liu, H., Hu, W-B., et al. (2018). Engineering oxygen vacancy on NiO nanorod arrays for alkaline hydrogen evolution. *Nano Energy* 43, 103–109. doi:10.1016/j.nanoen.2017.11.015

Zhang, W., Han, N., Luo, J., Han, X., Feng, S., Guo, W., et al. (2022). Critical role of phosphorus in hollow structures cobalt-based phosphides as bifunctional catalysts for water splitting. *Small* 18, 2103561. doi:10.1002/smll.202103561

Zhong, H., Gao, G., Wang, X., Wu, H., Shen, S., Zuo, W., et al. (2021). Ion irradiation inducing oxygen vacancy-rich NiO/$NiFe_2O_4$ heterostructure for enhanced electrocatalytic water splitting. *Small* 17, 2103501. doi:10.1002/smll.202103501

Zhu, J., Hu, L., Zhao, P., Lee, L. Y. S., and Wong, K-Y. (2020). Recent advances in electrocatalytic hydrogen evolution using nanoparticles. *Chem. Rev.* 120, 851–918. doi:10.1021/acs.chemrev.9b00248

Zhu, K., Shi, F., Zhu, X., and Yang, W. (2020). The roles of oxygen vacancies in electrocatalytic oxygen evolution reaction. *Nano Energy* 73, 104761. doi:10.1016/j.nanoen.2020.104761